

## HIGH-PRECISION LIMB-DARKENING MEASUREMENT OF A K3 GIANT USING MICROLENSING

DALE L. FIELDS,<sup>1</sup> M. D. ALBROW,<sup>2,3</sup> J. AN,<sup>1,4</sup> J.-P. BEAULIEU,<sup>5</sup> J. A. R. CALDWELL,<sup>6</sup> D. L. DEPOY,<sup>1</sup> M. DOMINIK,<sup>7</sup>  
B. S. GAUDI,<sup>8,9</sup> A. GOULD,<sup>1</sup> J. GREENHILL,<sup>10</sup> K. HILL,<sup>10</sup> U. G. JØRGENSEN,<sup>11</sup> S. KANE,<sup>7</sup> R. MARTIN,<sup>12</sup>  
J. MENZIES,<sup>6</sup> R. W. POGGE,<sup>1</sup> K. R. POLLARD,<sup>2</sup> P. D. SACKETT,<sup>13</sup> K. C. SAHU,<sup>3</sup> P. VERMAAK,<sup>6</sup>  
R. WATSON,<sup>10</sup> AND A. WILLIAMS<sup>12</sup> (THE PLANET COLLABORATION)

AND

J.-F. GLICENSTEIN<sup>14</sup> AND P. H. HAUSCHILDT<sup>15</sup>

Received 2003 March 28; accepted 2003 July 1

### ABSTRACT

We obtain high-precision limb-darkening measurements in five bands ( $V$ ,  $V_E$ ,  $I_E$ ,  $I$ , and  $H$ ) for the K3 III ( $T_{\text{eff}} = 4200$  K,  $[\text{Fe}/\text{H}] = +0.3$ ,  $\log g = 2.3$ ) source of the Galactic bulge microlensing event EROS BLG-2000-5. These measurements are inconsistent with the predictions of atmospheric models at higher than  $10\sigma$ . While the disagreement is present in all bands, it is most apparent in  $I$ ,  $I_E$ , and  $V_E$ , in part because the data are better and in part because the intrinsic disagreement is stronger. We find that when limb-darkening profiles are normalized to have unit total flux, the  $I$ -band models for a broad range of temperatures all cross each other at a common point. The solar profile also passes through this point. However, the profile as measured by microlensing does not. We hypothesize that the models have incorporated some aspect of solar physics that is not shared by giant atmospheres.

*Subject headings:* gravitational lensing — stars: atmospheres

### 1. INTRODUCTION

The brightness profiles (limb darkenings) of stars are a potentially powerful probe of their atmospheres as a function of depth. At each point along the projected radius of a star, the observed flux originates from a range of physical depths, the deepest of which (the surface of last scattering) increases with projected physical radius as one's line of sight progresses from the center of the star toward its limb. Hence, since stellar temperatures generally fall towards the surface, one expects that the limb will appear cooler (and therefore redder and fainter) than the center. If model atmospheres accurately reflect the physical conditions of the star as a function of depth, they should reproduce the star's limb-darkening profile.

Because limb darkening is a photometric quantity, it can, in principle, be measured to high precision. The drawback is that one has to be able to determine where on the star the light is coming from. Historically, there are two ways this is done. The first is resolving the star. The most obvious example would be the Sun (Pierce & Waddell 1961). Recent advances in interferometry have allowed one to resolve the surfaces of the highest angular diameter stars (Burns et al. 1997) and have in recent years provided data good enough to begin challenging models (Wittkowski et al. 2001). The second method is by occultation, either by an object in our solar system or by one orbiting the observed star. The Moon is the only occulter used in our solar system. However, while lunar occultations are sufficiently precise to demonstrate that limb-darkened models are superior to uniform-brightness models, they lack the precision to test limb-darkening models. If the occulting body is in the source's system, it can be a star or a planet. If it is a star, the system is more properly referred to as an eclipsing binary. While such systems would seem to have great potential, it is extremely difficult to disentangle the limb-darkened profile from other parameters describing the fit to an eclipsing-binary light curve (Popper 1984, 1985). The first extrasolar transiting planet to be discovered is HD 209458b (Charbonneau et al. 2000). Because the planet is much smaller and darker than the star, its transits can be used to trace the stellar light profile in great detail (Brown et al. 2001). Moreover, it is generally expected that ongoing and future transit surveys will turn up several more such systems.

There is one other method that can distinguish between light coming from different parts of a star. If a star passes through a microlensing pattern, different parts of the star are magnified by different amounts. In practice, differential magnification is significant only when the star passes through a caustic, which is a region of formally infinite magnification for a point source. Up to now, the best measurement of microlens limb darkening has been from MACHO 97-BLG-28 (Albrow et al. 1999a). This is because the event included a cusp crossing and thus the magnification pattern

<sup>1</sup> Department of Astronomy, Ohio State University, 140 West 18th Avenue, Columbus, OH 43210; fields@astronomy.ohio-state.edu.

<sup>2</sup> Department of Physics and Astronomy, University of Canterbury, Private Bag 4800, Christchurch, New Zealand.

<sup>3</sup> Space Telescope Science Institute, 3700 San Martin Drive, Baltimore, MD 21218.

<sup>4</sup> Institute of Astronomy, University of Cambridge, Madingley Road, Cambridge CB3 0HA, UK.

<sup>5</sup> Institut d'Astrophysique de Paris, INSU-CNRS, 98 bis Boulevard Arago, F 75014 Paris, France.

<sup>6</sup> South African Astronomical Observatory, P.O. Box 9, Observatory 7935, South Africa.

<sup>7</sup> School of Physics and Astronomy, University of St. Andrews, North Haugh, St. Andrews, Fife KY16 9SS, UK.

<sup>8</sup> School of Natural Sciences, Institute for Advanced Study, Einstein Drive, Princeton, NJ 08540.

<sup>9</sup> Hubble Fellow.

<sup>10</sup> Physics Department, University of Tasmania, G.P.O. 252C, Hobart, Tasmania 7001, Australia.

<sup>11</sup> Astronomical Observatory, Niels Bohr Institute, Juliane Maries Vej 30, 2100 Copenhagen, Denmark.

<sup>12</sup> Perth Observatory, Walnut Road, Bickley, Western Australia 6076, Australia.

<sup>13</sup> Research School of Astronomy and Astrophysics, Australian National University, Mount Stromlo, Weston ACT 2611, Australia.

<sup>14</sup> DAPNIA-SPP, CE-Saclay, F-91191 Gif-sur-Yvette, France.

<sup>15</sup> Universität Hamburg, Hamburger Sternwarte, Gojenbergsweg 112, D-21029 Hamburg, Germany.

was sharper, thereby giving better resolution across the star. In addition, the data for this event are very good. Albrow et al. (1999a) were able to measure two limb-darkening parameters each in  $V$  and  $I$  for the K giant source. They demonstrated that the resulting surface profiles are in reasonable agreement with the predictions of atmospheric models for stars of the same spectral type. However, they were not able to challenge these models.

Afonso et al. (2000) obtained a linear limb-darkening coefficient in each of four bands for an A star in the Small Magellanic Cloud (MACHO 98-SMC-1). They confirmed the expected trend of increased limb darkening toward the blue, but the measurements are not precise enough to challenge models. The primary difficulty is that the source star is extremely faint,  $I \sim 22$ , so that even when it is highly magnified, the signal-to-noise ratio (S/N) is modest.

Albrow et al. (2000) obtained linear limb-darkening coefficients for a red clump giant (MACHO 97-BLG-41). Even though the event itself was quite favorable, with three caustic crossings and a cusp crossing, bad weather and bad luck combined to limit the sensitivity of the data to limb darkening.

The limb-darkening analysis of OGLE-1999-BUL-23 by Albrow et al. (2001) was a major breakthrough in this subject. They developed a method to simultaneously compare limb-darkening measurements in two bands ( $V$  and  $I$ ) with the predictions of a whole suite of atmospheric models. The analysis demonstrated a conflict only at the  $2\sigma$  level, so no significant conclusions could be drawn. However, if the density of measurements had been higher or the errors smaller, this technique would have been able to give observational input into atmospheric modeling of the limb darkening of a moderately evolved star for the first time.

The binary-lens microlensing event EROS BLG-2000-5 provides the best constraints on limb darkening by any microlensing event. This event has a caustic crossing that is 4 days long. This extraordinarily long timescale and the generally excellent weather for all 4 days at all five observatories combine to yield an extremely high density of coverage of the source crossing in units of its own radius. The first caustic crossing is well measured (fortuitously, since its onset cannot be predicted beforehand), and the event contains a cusp approach in addition to the two caustics. Hence, this event is better constrained than any other microlensing event (An et al. 2002). With the physical parameters of the event well constrained, higher order terms in the microlensing parameterization such as limb darkening can be precisely determined. In fact, An et al. (2002) derive a two-parameter limb-darkening model as part of their general solution, but only for  $I$  band, to which their analysis is restricted.

We are not the first, then, to provide high-precision measurements of limb darkening in stars, let alone giants. Both Albrow et al. (1999a) and Wittkowski et al. (2001) have done so using microlensing and interferometry, respectively. In addition, both showed that the atmospheric models give good predictions as to the limb darkening of their respective stars. However, neither of these studies compared the models with the data in a parameterized space that was capable of challenging the models. For example, Wittkowski et al. (2001) shows that the limb-darkening models for his stars are preferred over models of stars of different spectral type, but he does not perform the analysis in a space for which the models and the data are independent

of each other. Conversely, Albrow et al. (2001) contrast the models and the data in a space for which both quantities are independent of each other, but the data are not of sufficient precision to confront the models. For the first time we present an analysis that is capable of challenging the atmospheric models with data good enough to do the job.

We extend the  $I$ -band analysis of An et al. (2002) to encompass four additional filters ( $V$ ,  $V_E$ ,  $I_E$ , and  $H$ ). In addition, we have spectroscopic data for this star (taken when it was highly magnified) that give us independent information about its temperature, metallicity, and surface gravity. This combination of information allows us to confront model atmospheres of what we determine to be a K3 III star in all five bands. We test the Kurucz ATLAS models (Claret 2000) in the Johnson-Cousins  $V$ ,  $I$ , and  $H$  bands, and the Hauschildt Next<sup>2</sup>Gen models in the same Johnson-Cousins bands plus two nonstandard bands,  $V_E$  and  $I_E$ . (The Next<sup>2</sup>Gen models are the current versions of the Next-Gen models described in Hauschildt et al. 1999a, 1999b.)

## 2. DATA

In our analysis of EROS BLG-2000-5 we make use of 11 data sets in five filters. The PLANET collaboration contributes nine data sets in three standard filters: three sets in  $V$ , four in  $I$ , and two in  $H$ . A description of the  $I$ -band data can be found in An et al. (2002). The  $V$ -band data are very similar in quality to the  $I$ -band, the main difference being that they contain about half the number of points. The  $H$ -band data were taken at SAAO and YALO by the instruments DANDICAM and ANDICAM, respectively. The instruments and procedures are identical in these two cases, and each contains a Tektronix  $2048 \times 2048$  CCD and a Rockwell  $1024 \times 1024$  HgCdTe IR array. The light path contains a dichroic that allows optical and near-IR images to be obtained simultaneously at the same position on the sky. The  $H$ -band images are constructed by averaging five contiguous dithered frames of 60 s each. The dithered images are flat-field-corrected and then used to create a median sky image, which is subtracted from the individual frames before they are shifted and co-added. The last two data sets are from the EROS collaboration and are those described in Afonso et al. (2003). The data are taken in  $V$ -like and  $I$ -like bands ( $V_E$  and  $I_E$ ), which are more fully described in Afonso et al. (2001). The data reduction for the SAAO ( $V$ ,  $I$ , and  $H$ ), and YALO ( $V$ ,  $I$ , and  $H$ ) is done using DoPHOT (Schechter, Mateo, & Saha 1993). The EROS data are reduced using PEIDA (Ansari 1996) and are more fully described in Afonso et al. (2003). Difference imaging primarily using ISIS (Alard 2000) improves the Canopus ( $V$  and  $I$ ) and Perth ( $I$  only) photometry, and so this method is carried out for these three data sets. In the same manner as An et al. (2002), each data set is cleaned of bad points by removing those with such high  $\chi^2$  that they are inconsistent with any model. Note that the number of points in the PLANET  $I$ -band data sets may be individually different from that given in An et al. (2002), as these cuts were done independently. However, since the total difference is only 10 points out of 1287, the impact on our conclusions is negligible. Finally, each data set has its errors rescaled so that the reduced  $\chi^2$  is unity for the best-fit model. The attributes of the data sets are given in Table 1.

TABLE 1  
DATA SETS

Band	Observatory	Number of Points	$\sigma$ Scaling
$V$ .....	SAAO	177	1.46
	Canopus	154	1.96
	YALO	233	1.23
$V_E$ .....	EROS	830	1.59
$I_E$ .....	EROS	904	1.66
$I$ .....	SAAO	404	1.75
	Canopus	311	2.73
	YALO	424	1.59
$H$ .....	Perth	148	2.77
	SAAO	549	2.47
	YALO	659	1.94

## 3. MODEL

We continue the model formalism of An et al. (2002), which contains 11 geometric parameters. Seven of these are static binary lens parameters: the lens separation in units of the Einstein radius  $d_{lc}$  (hereafter simply  $d$ ), the binary lens mass ratio  $q$ , the angle between the direction of motion of the source and the binary lens axis  $\alpha'$ , the distance between the cusp and the source at closest approach  $u_c$ , the time taken to travel an Einstein radius  $t'_E$ , the time of closest approach to the cusp  $t_c$ , and the ratio of source radius to Einstein radius  $\rho_*$ . Two are rotational parameters,  $\dot{d}$  and  $\omega$ , and two are vector components of microlens parallax,  $\pi_{E,\parallel}$  and  $\pi_{E,\perp}$ . The derivation of this parameterization and its relation to the standard formalism is given in An et al. (2002). Our geometric solution and that of An et al. (2002) are given in Table 2.

In addition, each observatory and band has its own five photometric parameters: the unmagnified source flux  $f_s$ , the blend flux  $f_b$ , a linear seeing correction  $\eta_s$ , a linear limb-darkening parameter  $\Gamma$ , and a square root limb-darkening parameter  $\Lambda$ . These photometric parameters are returned from a linear fit to the magnification curve determined by the 11 geometric parameters. For each band ( $V$ ,  $I$ , and  $H$ ) that is observed from several observatories, all observatories are constrained to give the same values of  $\Gamma$  and  $\Lambda$ .

TABLE 2  
MODEL PARAMETERS FOR EROS BLG-2000-5

Parameter	Joint Solution	An et al. (2002)
$d$ .....	1.940	$1.928 \pm 0.004$
$q$ .....	0.75	$0.7485 \pm 0.0066$
$\alpha'$ .....	$73^{\circ}851151$	$74^{\circ}18 \pm 0^{\circ}41$
$u_c$ .....	$-5.096 \times 10^{-3}$	$(-5.12 \pm 0.03) \times 10^{-3}$
$t'_E$ (days).....	100.371	$99.8 \pm 1.5$
$t_c^a$ .....	1736.941939	$1736.944 \pm 0.005$
$\rho_*$ .....	$4.767 \times 10^{-3}$	$(4.80 \pm 0.04) \times 10^{-3}$
$\pi_{E,\parallel}$ .....	-0.193073	$-0.165 \pm 0.042$
$\pi_{E,\perp}$ .....	0.195951	$0.222 \pm 0.031$
$\dot{d}$ ( $\text{yr}^{-1}$ ).....	0.280	$0.203 \pm 0.016$
$\omega$ ( $\text{yr}^{-1}$ ).....	0.0157	$0.006 \pm 0.076$

<sup>a</sup> Heliocentric Julian Date - 2,450,000.

The form of the limb-darkening law we use is

$$S_{\lambda}(\vartheta) = \bar{S}_{\lambda} \left[ (1 - \Gamma_{\lambda} - \Lambda_{\lambda}) + \frac{3\Gamma_{\lambda}}{2} \cos \vartheta + \frac{5\Lambda_{\lambda}}{4} \sqrt{\cos \vartheta} \right], \quad (1)$$

which conserves flux independent of  $\Gamma$  and  $\Lambda$ , with  $\bar{S}_{\lambda}$  being the mean surface brightness of the source and  $\vartheta$  the angle between the normal to the stellar surface and the line of sight. This law is a different form of the more widely used one,

$$S_{\lambda}(\vartheta) = S_{\lambda}(0) [1 - c_{\lambda}(1 - \cos \vartheta) - d_{\lambda}(1 - \sqrt{\cos \vartheta})]. \quad (2)$$

It should be noted, however, that equation (2) is normalized to the flux at the center, and thus the total flux is a function of  $S_{\lambda}(0)$ ,  $c_{\lambda}$ , and  $d_{\lambda}$ .

The transformation of the coefficients in equation (1) to the usual coefficients used in equation (2) is given by

$$c_{\lambda} = \frac{6\Gamma_{\lambda}}{4 + 2\Gamma_{\lambda} + \Lambda_{\lambda}}, \quad d_{\lambda} = \frac{5\Lambda_{\lambda}}{4 + 2\Gamma_{\lambda} + \Lambda_{\lambda}}, \quad (3)$$

while the inverse transformation is

$$\Gamma_{\lambda} = 10c_{\lambda}/(15 - 5c_{\lambda} - 3d_{\lambda})$$

and

$$\Lambda_{\lambda} = 12d_{\lambda}/(15 - 5c_{\lambda} - 3d_{\lambda}).$$

The limb-darkening parameters are primarily determined by the behavior of the light curve between the time the source edge enters the caustic and the time the source center enters the caustic (and the inverse of this process as the source leaves the caustic).

We then take this model and expand it to include all five bands, constraining all observations in the same band to give the same limb-darkening parameters. However, since there are no seeing data for EROS, these two bands do not have seeing corrections. This gives our model a total of 11 geometric plus (5 photometric  $\times$  11 data sets - 2 EROS seeing coefficients) = 64 fit parameters, which are then subject to  $(2V + 3I + 1H) \times 2$  limb-darkening parameters = 12 constraints.

## 4. ANALYSIS

4.1.  $\chi^2$  Minimization

The division of the model parameters into two categories, geometric and photometric, takes on additional significance when we search for a minimum in the  $\chi^2$  surface of the microlens model. A best fit can always be algebraically made to a linear equation. Unfortunately, the microlens model contains nonlinear parameters, for which a separate method must be applied. We therefore perform a grid search over the nonlinear (geometric) parameters, solving for the linear (photometric) parameters at each fixed geometry. This hybrid technique has the advantage of varying over all the parameters simultaneously, while still retaining the direct minimization of the linear parameters.

We employ a simple grid-search algorithm and not a more efficient technique such as simplex to minimize over the 11 geometric parameters because the (apparent)  $\chi^2$  surface is rough, with many false minima. This problem forces

us to restrict our automated grid search to nine of the geometric parameters at each fixed  $(d, q)$ . At each  $(d, q)$  we initialize the other nine geometric parameters, as well as the step size in those parameters. We then vary 0, 1, and 2 parameters at a time, calculating  $\chi^2$  at each of these 163 geometries. The “central” geometry is then set to be that with the lowest  $\chi^2$ , and the variation begins again. If none of the neighboring geometries have a lower  $\chi^2$ , the step sizes for all parameters are cut in half, and the grid search proceeds again. The minimization is declared complete after a user-defined number of cuts in the step sizes. This is done to avoid descent into numerical noise. We then reinitialize the routine at another  $(d, q)$ , and in this manner step through the  $(d, q)$  grid “by hand.”

Even so, we find that we can locate the true minimum only to within  $\sim 0.02$  in  $d$  and  $q$ , despite the fact that the true errors in these parameters (as determined from the curvature of the  $\chi^2$  surface measured over larger scales) are less than 0.01; that is, the apparent  $\chi^2$  varies by  $\sim 10$  for the same  $(d, q)$  when we initialize our search using different values of the other nine parameters. We believe that this roughness is most likely due to numerical noise rather than roughness in the “true”  $\chi^2$  surface. However, regardless of the exact cause of the roughness of the surface, its impact via increased uncertainty in  $(d, q)$  on the errors in the limb-darkening parameters must be assessed. This will be done in § 4.2.

We start the grid search at the minimum found by An et al. (2002). This is reasonable as An et al. (2002) find limb darkening in the  $I$  band with a subset of our data. To save computation cycles, we first do a grid search using only  $I$ -,  $I_E$ -, and  $H$ -band data. After the new minimum has been approximately located, the  $V$ - and  $V_E$ -band data are finally included. The limb darkening of the best-fit microlens model is shown in Figure 1.

#### 4.2. Errors

Contributions to the error in the limb-darkening parameters can be broken down into three sources: the photometric (which include limb-darkening) parameters, the geometric parameters minimized over in our automated routine, and  $d$  and  $q$ . The covariance matrix from the photometric parameters is easily obtained, as it is a by-product of the linear fit that solves for the photometric parameters. We then apply the hybrid statistical error analysis as given in Appendix D of An et al. (2002) to determine the combined covariance matrix for the nine geometric plus 55 photometric parameters. While this approach does yield an invertible covariance matrix, there are reasons not to trust this method in this particular instance. We have stated above in § 4.1 that the apparent  $\chi^2$  surface is rough, with numerical noise a possible culprit. An effect of numerical noise on the ideal  $\chi^2$  parabola is to artificially raise the  $\chi^2$  at any particular point in parameter space. This is illustrated in Figure 2. A good approximation to the true (numerical noise-free) parabola can be found by fitting to the outside envelope as noise will not decrease  $\chi^2$ . We fit with this method the error induced by the nine geometric parameters that we minimize over. As stated above in § 4.1, we have 163 geometries at each step in the grid-search algorithm, each of which has its own limb-darkening parameters and  $\chi^2$ . We use this as our input data set, fitting for each band separately. In all cases, we find that the  $\Gamma$ - $\Lambda$  error ellipse induced by the nine geometric

parameters is small compared with that induced by the photometric parameters. This implies that our somewhat ad hoc procedure for determining the geometry-induced errors does not significantly affect our overall error estimate. The two sets of error ellipses are well aligned, differing in orientation by only a few degrees. We add the resulting covariance matrices to obtain the geometric plus photometric errors.

Up to this point, we have not yet taken into account the error induced by  $d$  and  $q$ . The roughness of the  $\chi^2$  surface is also a factor in this analysis. Unfortunately, while it is theoretically possible to use the same method that we use on the other geometric parameters, it would take several orders of magnitude more computational resources than we currently have to properly populate the geometric figure analogous to Figure 2. We instead investigate whether and to what extent the additional error in our limb-darkening parameters induced by  $d$  and  $q$  will affect our conclusions.

To this end, we first define

$$(\Delta\chi^2)_{\text{LD}} = \sum_{ij} \delta a_i b_{ij} \delta a_j, \quad (4)$$

where  $\delta a_i$  is a vector whose components are the differences between the limb-darkening parameters of our best-fit model and a comparison model. Here  $b_{ij} \equiv (c_{ij})^{-1}$  and  $c_{ij}$  is the covariance matrix of the limb-darkening parameters evaluated at the best-fit model. We define equation (4) as  $\Delta\chi^2$  because it is the distance, expressed in  $\chi^2$  and normalized by the error ellipsoid, between models that both attempt to describe the data. We then compare our best-fit microlens model with other microlens models over the roughly  $(0.02 \times 0.02)$  region of the  $(d, q)$  space over which  $\chi^2$  cannot be properly minimized on account of the roughness in the  $\chi^2$  surface described in § 4.1. We find that the limb-darkening parameters vary by less than  $1 \sigma$ . By comparison, as we show in § 4.4 and § 4.5, the limb-darkening parameters of our best-fit model differ from those predicted by the stellar models by more than  $10 \sigma$ . We conclude that the additional errors resulting from both the uncertainty in  $d$  and  $q$  and the underlying numerical noise do not affect our overall conclusions. We recognize that this additional error exists, but given that we have no way to quantify it properly, we simply report the error induced by the photometric and other nine geometric parameters in Table 3.

#### 4.3. Independent Analysis of Source Star

When we compare our limb-darkening results with the atmospheric models in §§ 4.4 and 4.5, we wish to restrict attention to models that are relevant to the source star. We therefore begin by summarizing the results of an analysis of the source’s physical properties as given by An et al. (2002). Assuming no differential reddening across the field, the dereddened color and magnitude of the source can be found by measuring the source offset from the red clump identified in a color-magnitude diagram of the field:  $(V-I)_0 = 1.390 \pm 0.010$  and  $I_0 = 14.70 \pm 0.03$ . From its color and the fact that it is a giant (see below), the source is a K3 III star with a corresponding  $T_{\text{eff}} = 4200$  K. The color and magnitude imply a source angular radius  $\theta_* = (6.62 \pm 0.58) \mu\text{as}$ . The source-lens relative proper motion and source radial velocity imply that the source most probably lies in the bulge, i.e., at  $d_s \sim 8$  kpc, which implies a physical radius  $r_* = d_s \theta_* = 11.4 \pm 1.0 R_\odot$ . From kinematic information, An et al. (2002) find that

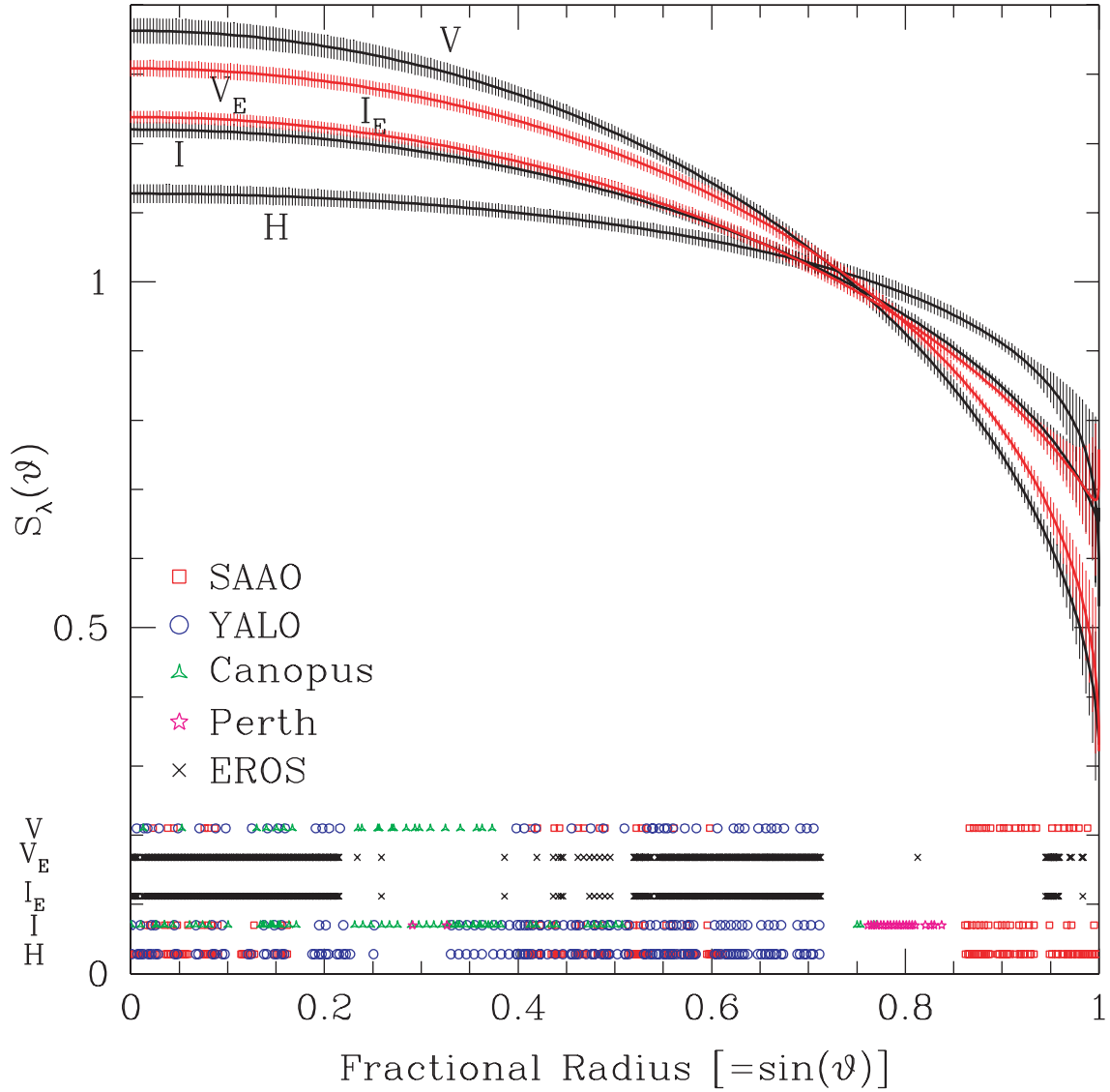


FIG. 1.—Derived brightness profiles for the source star of EROS BLG-2000-5 in all five bands,  $V$ ,  $V_E$ ,  $I_E$ ,  $I$ , and  $H$ . The shaded regions around the curves are the  $3\sigma$  error envelopes. Also shown are points indicating when data were taken at each observatory, expressed in distance from the caustic to the center of the source in units of the source radius. At this point, the magnification pattern over the source profile is discontinuous, which gives us precise information about the profile at that point. For example, since the  $I$  band has almost continuous coverage across the entire source star, we can be confident that the brightness profile well represents reality. The  $V$  and  $H$  bands have a gap in coverage around  $\sin \vartheta = 0.8$ , and thus we can be less confident of the profile there. The EROS data, produced by a single observatory, have large gaps but are still able to make the two-parameter fit on account of their very dense coverage when the observatory was active.

TABLE 3  
LIMB-DARKENING PARAMETERS, ERRORS, AND CORRELATION COEFFICIENTS

Parameter	$V$ Band	$V_E$ Band	$I_E$ Band	$I$ Band	$H$ Band
$\Gamma$ .....	$0.7856 \pm 0.1058$	$0.5500 \pm 0.0979$	$0.7280 \pm 0.0884$	$0.5622 \pm 0.0861$	$0.0252 \pm 0.1103$
$\Lambda$ .....	$-0.1192 \pm 0.1981$	$0.1342 \pm 0.1919$	$-0.5029 \pm 0.1772$	$-0.2434 \pm 0.1680$	$0.4598 \pm 0.2141$
$\tilde{c}_{ij}$ .....	$-0.9950$	$-0.9969$	$-0.9978$	$-0.9964$	$-0.9970$
$\varphi^a$ .....	$-61^\circ 96$	$-63^\circ 02$	$-63^\circ 52$	$-62^\circ 92$	$-62^\circ 79$
$\Gamma_I \cos \varphi + \Lambda_I \sin \varphi^b$ .....	$0.4745 \pm 0.2243$	$0.1299 \pm 0.2153$	$0.7747 \pm 0.1979$	$0.4726 \pm 0.1886$	$-0.3974 \pm 0.2408$
$\Lambda_I \cos \varphi - \Gamma_I \sin \varphi^c$ .....	$0.6374 \pm 0.0093$	$0.5510 \pm 0.0069$	$0.4275 \pm 0.0053$	$0.3898 \pm 0.0065$	$0.2326 \pm 0.0075$

<sup>a</sup> Location of major axis of error ellipse.

<sup>b</sup> Rotational transformation that maximizes the variance.

<sup>c</sup> Rotational transformation that minimizes the variance.

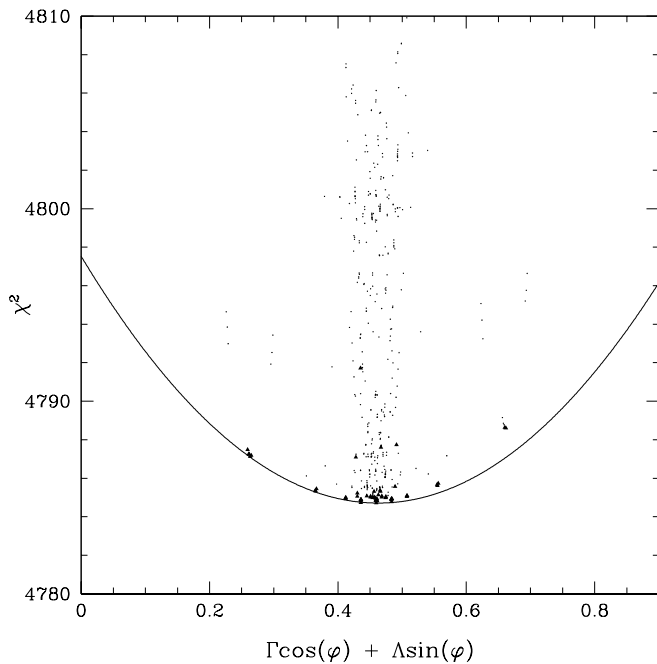


FIG. 2.—*I*-band  $\chi^2$  surface plotted as  $(\Gamma, \Lambda, \chi^2)$  and viewed along the minor axis of the error ellipse. Each point represents a slightly varied geometry and its associated  $\chi^2$  and limb-darkening parameters. The filled triangles are those points we use to create the covariance matrix. The parabola is the cut through the geometric error paraboloid for this particular viewing angle. Numerical noise will lift points in  $\chi^2$  at a particular  $(\Gamma, \Lambda)$  and is responsible for the larger  $\chi^2$  among those points that we do not use. Note that as the points are seen in projection and the paraboloid in section, the apparent elevation of the points is a combination of noise and projection effects.

while it is possible that the source lies in the far disk (and so is physically bigger), it essentially cannot lie in the near disk. Since the source is either in the bulge or in the far disk  $\sim 500$  pc above the plane, it must be a fairly old giant and therefore have a mass  $M \sim 1 M_{\odot}$ . The mass and radius combine to give  $\log g \sim 2.3$ . If it lies in the far disk at 12 kpc then  $\log g$  can be as much as 0.3 dex smaller.

S. I. Ramírez, S. Castro, & R. M. Rich (2003, in preparation) have analyzed High-Resolution Echelle Spectrograph Keck spectra taken by Castro et al. (2001), on the last two nights of the caustic crossing, HJD 2,451,731.953 and HJD 2,451,732.950, when the source center was approximately 0.25 and 0.75 source radii outside the caustic, respectively. First, they estimate the microturbulence for a set of  $T_{\text{eff}}$  and  $\log g$  models, requiring that the Fe abundance computed from the Fe I lines be independent of the strength of the lines. Then for each gravity they determine a  $T_{\text{eff}}$  requiring that the Fe abundance computed from the Fe I lines be independent of the excitation potential of the lines. Then, they compute the Fe abundance from Fe II at those  $T_{\text{eff}}$  and microturbulence, varying  $\log g$ , and finally they determine  $\log g$  by requiring no difference in the Fe abundance between the Fe I and Fe II lines.

They estimate  $T_{\text{eff}} = 4250$  K,  $\log g = 1.75$ ,  $[\text{Fe}/\text{H}] = +0.29 \pm 0.04$ , and  $v_T = 1.19$  on the first night and  $T_{\text{eff}} = 4450$  K,  $\log g = 2.25$ ,  $[\text{Fe}/\text{H}] = +0.22 \pm 0.07$ , and  $v_T = 1.77$  on the second. The gravity is too loosely constrained in this analysis to be of any use, but fortunately we have the photometric method applied to the An et al. (2002) results given above, which is both simpler and more robust.

Because the source is differentially magnified while the models are not, this spectroscopic approach is not fully self-consistent. Nevertheless, we expect the error induced to be modest, particularly on the first night when the limb of the star is not particularly emphasized in the integrated source light. Since, in addition, both the observing conditions and S/N were substantially better the first night, we adopt  $T_{\text{eff}} = 4250$  K and  $[\text{Fe}/\text{H}] = +0.3$  as the spectroscopic determinations. The former is in excellent agreement with the photometric determinations described above. We designate the model for which  $T_{\text{eff}} = 4200$  K,  $[\text{Fe}/\text{H}] = +0.3$ , and  $\log g = 2.3$  as the most physical model (MPM).

If we are to use these estimates to define a viable region of model-atmosphere parameter space, we need error estimates as well. High-resolution spectroscopic temperature estimates are routinely good to 100 K. Similarly, our photometric temperature estimate can be off by a 100 K, depending on differential reddening. As summarized above, the source gravity is strongly constrained by the angular size measurement and distance estimates. One could possibly push the source into the near part of the bulge, or into the far disk, but that is all. There is also some error associated with the mass estimation, but because of age constraints the mass cannot be too far from  $\sim 1 M_{\odot}$ . We budget a 20% mass error, corresponding to an age range of 4–16 Gyr, which should encompass the great majority of bulge stars. Considering all such errors gives us the range  $\log g = 2.3^{+0.3}_{-0.4}$ . The metallicity is the least well constrained. This is only a minor problem, for, as we show in §§ 4.4 and 4.5, metallicity has only a minor effect on the model atmosphere limb-darkening curves. We set our lower metallicity limit at solar. Physically reasonable models (PRMs) would then have  $T_{\text{eff}} = 4100\text{--}4300$  K,  $\log g = 1.9\text{--}2.6$ , and  $[\text{Fe}/\text{H}] = 0.0$  to  $+0.3$ .

#### 4.4. Comparison with ATLAS Models

Claret (2000) fits five different limb-darkening laws to a suite of ATLAS model atmospheres supplied to him by R. Kurucz in 2000. Claret (2000) then reports the parameters for each of these limb-darkening laws. We compare our results with the linear plus square root law, rather than the favored four-parameter fit since we also use a linear plus square root law in our fitting, and thus the coefficients are comparable. Little is lost by this substitution, as the four-parameter and two-parameter fits differ by much less than the difference between the microlensing-based and atmospheric model profiles. We use equation (4) to create our measure of goodness of fit, but because we are now comparing theoretical atmospheric models with what we consider a parameterization of reality, we term the result “ $\chi^2$ ” rather than “ $\Delta\chi^2$ .” Equation (4) implicitly assumes that the  $\chi^2$  surface is parabolic, which, since the microlensing fit is non-linear, is not strictly the case. However, as shown in § 4.2, the covariance matrix is dominated by the linear part of the fit. Hence, the  $\chi^2$  surface is nearly parabolic. As before,  $\delta a_i$  is a difference in the limb-darkening parameters, this time between an atmospheric model and our microlensing result, and  $b_{ij}$  is the inverse of  $c_{ij}$ , the covariance matrix for the microlensing limb-darkening parameters. We convert the Claret (2000)  $c_{\lambda}$  and  $d_{\lambda}$  to  $\Gamma_{\lambda}$  and  $\Lambda_{\lambda}$  by using the inverse of equation (3) to make the comparison. We restrict the comparison to the standard (Johnson-Cousins) bands *V*, *I*, and *H*, because Claret (2000) reports limb-darkening parameters only for these.

Following the procedure pioneered by Albrow et al. (2001), we begin by simultaneously comparing the microlensing limb-darkening parameters from all three filters with the atmospheric model parameters, taking full account of the covariances among these six parameters. We restrict our investigation to those models with turbulent velocity  $v_T = 2$  only. Models given by Claret (2000) with other  $v_T$  do not span the full parameter space required by our investigation, nor do we have independent information that would distinguish among different  $v_T$  as we do for  $T_{\text{eff}}$ ,  $[\text{Fe}/\text{H}]$ , and  $\log g$ . Special attention is paid to two regions of the  $\chi^2$  surface: the neighborhood of the MPM to check for consistency between the atmospheric models and the microlens data, and features around  $\chi_{\text{min}}^2$  (which may not be near the MPM) to try to guide modelers in understanding the results of their simulations. The ATLAS parameter grid does not contain the MPM, but the closest is  $T_{\text{eff}} = 4250$  K,  $\log g = 2.5$ , and  $[\text{M}/\text{H}] = +0.3$ . We refer to this as the MPM while within § 4.4. In addition, the ATLAS models given in Claret (2000) have a larger grid spacing than the region covered by the PRMs, so we investigate  $T_{\text{eff}} = 4000\text{--}4500$  K,  $\log g = 2.0$  and  $2.5$ , and  $[\text{M}/\text{H}]$  from  $0.0$  to  $+0.3$ . We define consistency as having a  $\chi^2 \lesssim 4$ . We find that  $\chi^2$  at the MPM is 94. In fact, all the PRMs are high, with the lowest  $\chi^2$  among them at 38. This in itself is a major concern. That no model atmosphere agrees with our data, regardless of its parameters, is evident by the fact that  $\chi_{\text{min}}^2 = 36$ . This occurs at  $T_{\text{eff}} = 4500$  K,  $\log g = 2.5\text{--}3.5$ , and  $[\text{M}/\text{H}] = -0.1$  and  $-0.2$ , which is incompatible with the other evidence we have about this star. We find that, in all the ATLAS models in the vicinity of the MPM, the differences in  $\chi^2$  between  $\log g = 2.0$  and  $2.5$  are small compared with those induced by changes in the other two parameters. Across the PRMs, the magnitude of the change in  $\chi^2$  induced by  $T_{\text{eff}}$  is  $\sim 100$ , by metallicity,  $\lesssim 10$ , and by  $\log g$ ,  $\sim 1$ . This is not true in the case of the  $V$  and  $I$  bands, for which the effect of gravity is approximately equal to that of the metallicity. Because of this lack of distinguishing power in the surface gravity, we focus our investigation on  $\log g = 2.5$ . Any model whose gravity is not listed should be assumed to have  $\log g = 2.5$ . To determine whether the large mismatch in limb-darkening parameters comes primarily from one specific band, we investigate the goodness of fit for each band separately.

#### 4.4.1. $V$ Band

We repeat our  $\chi^2$  minimization over the space of ATLAS models, considering only the  $V$ -band parameters  $\Gamma_V$  and  $\Lambda_V$ . The MPM has a  $\chi^2$  of 20. We then look for PRMs that might be consistent. All points with  $T_{\text{eff}} = 4500$  K have  $\chi^2 < 4$  and are thus consistent. Because of the small spread in  $\chi^2$  within this sample (1.99–2.57), nothing can be said about favored values of  $[\text{M}/\text{H}]$  and  $\log g$ . It must be pointed out, however, that the grid spacing of the ATLAS models is larger than the true permitted temperature range. If we take this into account and note that at  $T_{\text{eff}} = 4250$  K,  $\chi^2 > 14$ , we must downgrade the  $V$  band to marginal inconsistency. The shape of the  $\chi^2$  surface near  $\chi_{\text{min}}^2$  returns a “valley” (part of which is shown in Fig. 3b) running along  $T_{\text{eff}} = 4500$  K. The  $V$  band has a greater dependence on  $\log g$  than the combined all-band  $\chi^2$  surface.

#### 4.4.2. $H$ Band

We perform an analysis for  $H$  band in the same manner as in the previous section. The MPM has  $\chi^2 = 2.7$ . About half the PRMs are consistent as well. This avoids the caveat we applied in the previous section (§ 4.4.1). The  $H$  band also has a valley structure (Fig. 3d) in its  $\chi^2$  surface analogous to that in the  $V$  band, although there is some dependence on  $T_{\text{eff}}$  in the range that we investigate. This  $T_{\text{eff}}$  dependence is slight; the location of the “valley floor” shifts from  $T_{\text{eff}} = 3500$  K at  $[\text{M}/\text{H}] = -1.0$  to  $T_{\text{eff}} = 4500$  K at  $[\text{M}/\text{H}] = +1.0$ . As in the all-band comparison,  $\log g$  is essentially unimportant in the  $H$  band.

#### 4.4.3. $I$ Band

The  $I$  band MPM has  $\chi^2 = 71$ . None of its PRMs are consistent with the microlens limb darkening; the lowest  $\chi^2$  among them is 28. The  $\chi_{\text{min}}^2$  over the entire space of  $I$ -band models is still moderately high at 13. In general, it is the  $I$  band that is causing most of the discrepancy between models and data. The atmospheric models that have the lowest  $\chi^2$  form a track in parameter space that varies smoothly from solar-metallicity dwarfs at  $T_{\text{eff}} \sim 4750$  K to super-metal-poor supergiants at  $T_{\text{eff}} = 3500$  K. As discussed in § 4.4, in this band, as in the  $V$  band, the effect of surface gravity on  $\chi^2$  is of the same magnitude as the effect of metallicity. What is interesting is that the sense is opposite between these two bands. The  $I$  band slightly prefers a lower gravity, while the  $V$  band slightly prefers a higher gravity. When then summed together with the  $H$  band, the resultant all-band  $\chi^2$  surface does not favor one gravity over the other.

At this point, we can ask whether the bands are consistent with each other. In a relative sense, they are, as the PRMs with the lowest  $\chi^2$  are always those with  $T_{\text{eff}} = 4500$  K, no matter the band. We defer discussion as to the possible causes of the disagreement between the ATLAS atmospheric models and the microlens data until § 4.6, after we have investigated the Next<sup>2</sup>Gen models.

### 4.5. Comparison with Next<sup>2</sup>Gen Models

We analyze the limb darkening of Next<sup>2</sup>Gen models between  $T_{\text{eff}} = 4000$  and  $4600$  K in  $100$  K increments,  $\log g = 0.0$  and  $3.5$  in increments of  $0.5$ , and  $[\text{Fe}/\text{H}]$  of  $-0.25$ ,  $0.0$ , and  $+0.3$ . The original format of these files is a spectrum between  $3500$  Å and  $3$   $\mu\text{m}$  with a resolution of  $0.5$  Å at each of  $99$  points in  $\cos \vartheta$ .

Having the full spectra enables us to create limb-darkening profiles in nonstandard bands. We convolve the spectra with filter functions for all five filters in the microlens data ( $V$ ,  $V_E$ ,  $I_E$ ,  $I$ , and  $H$ ). We then use a simple linear fit to solve for the  $(\Gamma_\lambda, \Lambda_\lambda)$  for each filter.

The primary difficulty in this procedure is the definition of the edge of a star. The Next<sup>2</sup>Gen atmospheres have a steep drop-off in intensity whose location in radius varies with surface gravity. Sample profiles are shown in Figure 4. This feature cannot be modeled by a linear plus square root limb-darkening law, and because it contributes almost nothing to the total flux, we decide to remove it. This is further warranted because even if we had the formalism in our microlensing code to fit this feature, we would not receive any useful information since our sampling is not dense enough at the specific part of the caustic exit during which the feature would be visible. We therefore excise this feature

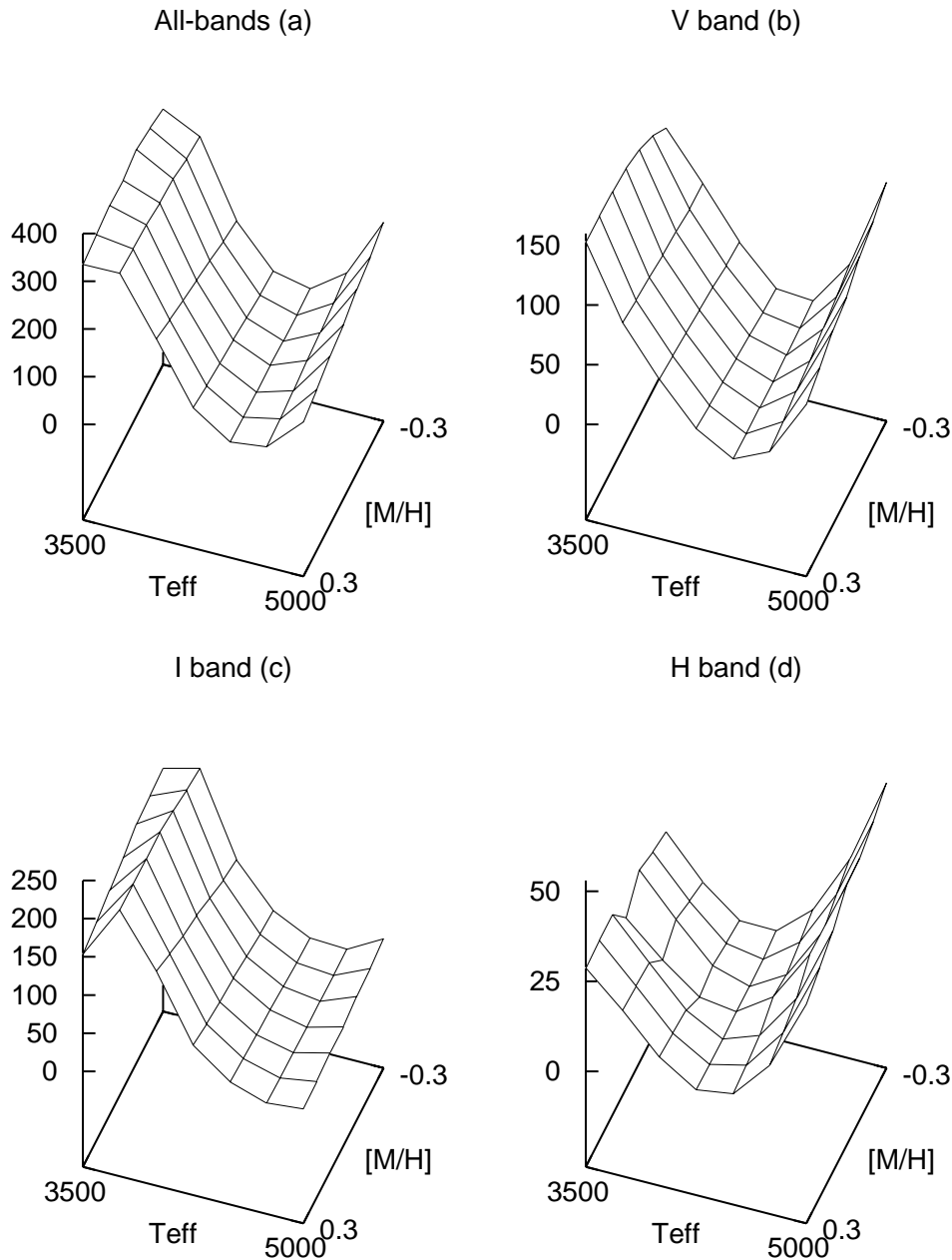


FIG. 3.— $\chi^2$  surfaces of the microlens-ATLAS comparison at  $\log g = 2.5$  for (a) the  $V$ ,  $I$ , and  $H$  bands combined, (b) the  $V$  band, (c) the  $I$  band, and (d) the  $H$  band. The value of  $\chi^2$  is most dependent on  $T_{\text{eff}}$  and less dependent on  $[M/H]$ . The dependence on  $\log g$  (not shown) is even weaker still. The surface of every band has a similar shape, a “valley” that runs through metallicity with almost constant  $T_{\text{eff}}$ . These structures mostly overlap, although the  $I$  band’s is shifted to slightly higher  $T_{\text{eff}}$ .

by removing all points outside some chosen radius. We then rescale the value of the radius at each remaining point by the factor necessary to set the outermost point’s radius equal to unity. The radius is chosen by finding the point at which the  $H$  band, which should suffer the least amount of limb darkening, drops steeply off. This is something of a judgment call, as individuals will pick slightly different truncation radii. This does not pose a problem, however, as tests indicate that the Next<sup>2</sup>Gen profile is equally well fitted by a two-parameter limb-darkening law out to radii somewhat beyond this steep drop-off in flux (but not into the feature we are removing). In the profiles shown in Figure 4, this occurs around  $r = 0.995$ , indicating that our cut at  $r = 0.993$  is acceptable. This procedure breaks down at low

surface gravity. Supergiants have such a small density gradient that the surface of last scattering at different wavelengths varies greatly with radius. This would be a major concern for us if we did not have additional information telling us that this star was a luminosity class III giant. We use a separate truncation radius at each  $\log g$  but not for each wavelength. Our adopted truncation radius varies between  $r = 0.88$  at  $\log g = 0.0$  to  $r = 0.998$  at  $\log g = 3.5$ . Having a single truncation radius for all bands would induce problems at the low  $\log g$  end, but such low surface gravities are already highly disfavored, as discussed in § 4.3.

In performing the fit, we sample the profile at the radii corresponding to the observations (see Fig. 1), giving equal weight to each point. We evaluate the profile at these radii

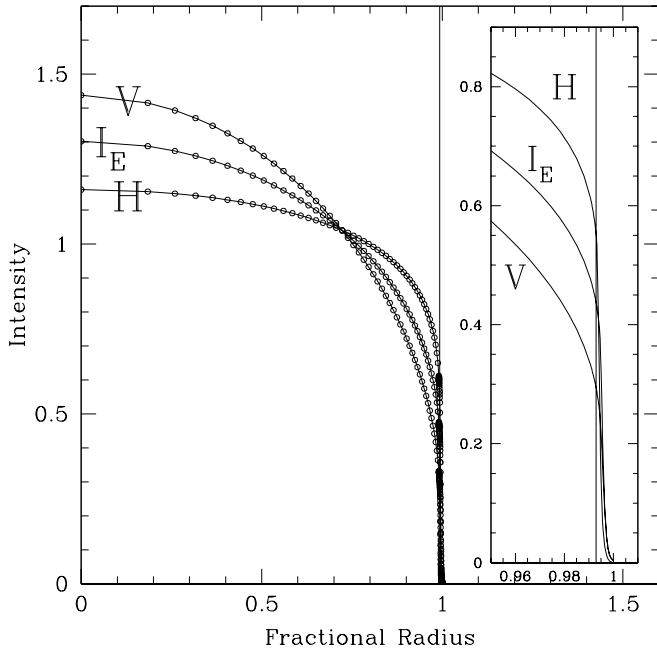


FIG. 4.—Sample limb-darkening profiles from the Next<sup>2</sup>Gen model corresponding to the MPM ( $T_{\text{eff}} = 4200$  K,  $\log g = 2.5$ ,  $[\text{Fe}/\text{H}] = +0.3$ ). Shown are the  $V$ ,  $I_E$ , and  $H$  bands. Each circle is a radial point in the Next<sup>2</sup>Gen output. Also shown is the cut in radius that we impose at  $r = 0.993$ .

by interpolating among the points given by the Next<sup>2</sup>Gen model. This produces a model profile that is most weighted in the regions that are most densely observed in the real data.

We then perform the same analysis as in § 4.4, creating a  $\chi^2$  surface between the microlens limb-darkening parameters and those of the Next<sup>2</sup>Gen models. The only difference is that we now have 10 limb-darkening parameters instead of six because we are also matching  $V_E$  and  $I_E$  in addition to  $V$ ,  $I$ , and  $H$ . As in the previous section, no grid points in parameter space for the Next<sup>2</sup>Gen models coincide perfectly with the MPM, and the grid spacing does not perfectly coincide with the range of the parameters covered by the PRMs. In this section we consider  $T_{\text{eff}} = 4200$  K,  $\log g = 2.5$ , and  $[\text{Fe}/\text{H}] = +0.3$  as the MPM, and we consider the range  $T_{\text{eff}} = 4100$  to  $4300$  K,  $\log g = 2.0$  and  $2.5$ , and  $[\text{Fe}/\text{H}] = 0.0$  to  $+0.3$  as that similar to our PRMs.

Turning now to the  $\chi^2$  analysis, the MPM is immediately ruled out:  $\chi^2 = 877$ . The PRMs are also ruled out, as the lowest  $\chi^2$  among them is 497. When we look over the entire parameter space, we find  $\chi_{\text{min}}^2 = 133$  at  $T_{\text{eff}} = 4600$  K,  $\log g = 2.5$ , and  $[\text{Fe}/\text{H}] = -0.25$ . From Figure 5a, it appears likely that the true  $\chi_{\text{min}}^2$  is outside the explored parameter space, at least in  $T_{\text{eff}}$ . There also appears to be a trend toward lower metallicity, so it is possible that the best-fit metallicity is also outside our explored parameter space. We discuss this further in § 4.6. In general,  $\chi^2$  increases with  $[\text{Fe}/\text{H}]$ , and decreases with  $T_{\text{eff}}$ . Surface gravities between  $\log g = 1.0$  and  $2.5$  are preferred, with higher  $T_{\text{eff}}$  and lower metallicity selecting for a higher  $\log g$ .

#### 4.5.1. Johnson-Cousins $V$ , $I$ , and $H$ Bands

At the MPM, the  $V$ ,  $I$ , and  $H$  bands have  $\chi^2 = 81$ , 136, and 21, respectively. Among the PRMs, all three bands prefer  $T_{\text{eff}} = 4300$  K and  $[\text{Fe}/\text{H}] = 0.0$ . A surface gravity of 2.5

is marginally preferred over 2.0 by the  $H$  band (the difference in  $\chi^2$  is  $\sim 3$ ), while the  $V$  and  $I$  bands do not significantly favor either gravity. The  $V$ ,  $I$ , and  $H$  bands have  $\chi^2$  at this PRM of 32, 99, and 15. The global minima for these bands are the following: for the  $V$  band,  $T_{\text{eff}} = 4600$  K,  $\log g = 3.5$ , and  $[\text{Fe}/\text{H}] = -0.25$ , with  $\chi_{\text{min}}^2 = 0.02$ ; for the  $I$  band,  $T_{\text{eff}} = 4600$  K,  $\log g = 2.5$ , and  $[\text{Fe}/\text{H}] = -0.25$ , with  $\chi_{\text{min}}^2 = 37$ ; and for the  $H$  band,  $T_{\text{eff}} = 4600$  K,  $\log g = 3.5$ , and  $[\text{Fe}/\text{H}] = -0.25$ , with  $\chi_{\text{min}}^2 = 1.14$ . In sum, the all-band and  $I$ -band minima coincide, and the  $\chi^2$  values for bands  $V$  and  $H$  at the all-band minimum are just  $\Delta\chi^2 \lesssim 0.5$  higher than at their own minima. That is, all three bands have the same minimum to within  $\sim 1 \sigma$ .

Qualitatively, this shape of the  $\chi^2$  surface is replicated for each individual band, as can be seen from Figure 5. One minor difference is that the  $V$ -band surface has more curvature in  $T_{\text{eff}}$  while in the other bands,  $\chi^2$  is approximately a linear function of  $T_{\text{eff}}$ . The other minor difference is that the  $H$  band favors high gravity independent of  $T_{\text{eff}}$ , while the other bands tend to favor a lower surface gravity at lower  $T_{\text{eff}}$ .

#### 4.5.2. EROS Bands $V_E$ and $I_E$

Each EROS band has a greater disagreement with every atmospheric model than any Johnson-Cousins band. The MPM has  $\chi^2 = 387$  and 251 for  $V_E$  and  $I_E$ , respectively. The best PRM for both bands is  $T_{\text{eff}} = 4300$  K,  $\log g = 2.0$ , and  $[\text{Fe}/\text{H}] = 0.0$ , with  $\chi^2 = 201$  and 146. The location of the  $\chi_{\text{min}}^2$  for the  $V_E$  and  $I_E$  bands is the same as for all bands, at  $T_{\text{eff}} = 4600$  K,  $\log g = 2.5$ , and  $[\text{Fe}/\text{H}] = -0.25$ , with  $\chi^2 = 47$  and 47.

#### 4.6. Possible Systematic Effects

Logically, there are only four possible sources for the discrepancy between the models and the data: (1) problems with the microlensing data, (2) problems with our analysis of the data, (3) problems with the atmosphere models, or (4) incorrect comparison of the models and the data. We now argue that (1), (2) and (4) are unlikely.

##### 4.6.1. Individual Observatories

We test whether the data from an individual observatory drives the combined solution to an unsuitable answer. We rerun our fitting routine five times at the  $(d, q)$  of the combined-band solution, each time removing a different observatory's data, the exception being that we always keep both  $H$ -band data sets. The removal of the SAAO, Perth, or EROS data sets does not appreciably change the limb-darkening curves. In the  $V$  band, the removal of the Canopus data shifts the limb-darkening parameters by approximately  $1 \sigma$ , and the removal of the YALO data shifts them by about  $3 \sigma$ . The reverse is true in the  $I$  band; removing the Canopus data provokes a  $3 \sigma$  change, while removing the YALO data induces only a  $1 \sigma$  change. This test shows that any systematic effects in the data themselves are either present in data sets across all observatories or are so mild that they do not affect the combined solution at the level of the difference between microlensing measurements and the atmospheric models.

##### 4.6.2. PLANET versus EROS Data Sets

We also analyze the solutions found by the PLANET data and EROS data separately. We expand the analysis to

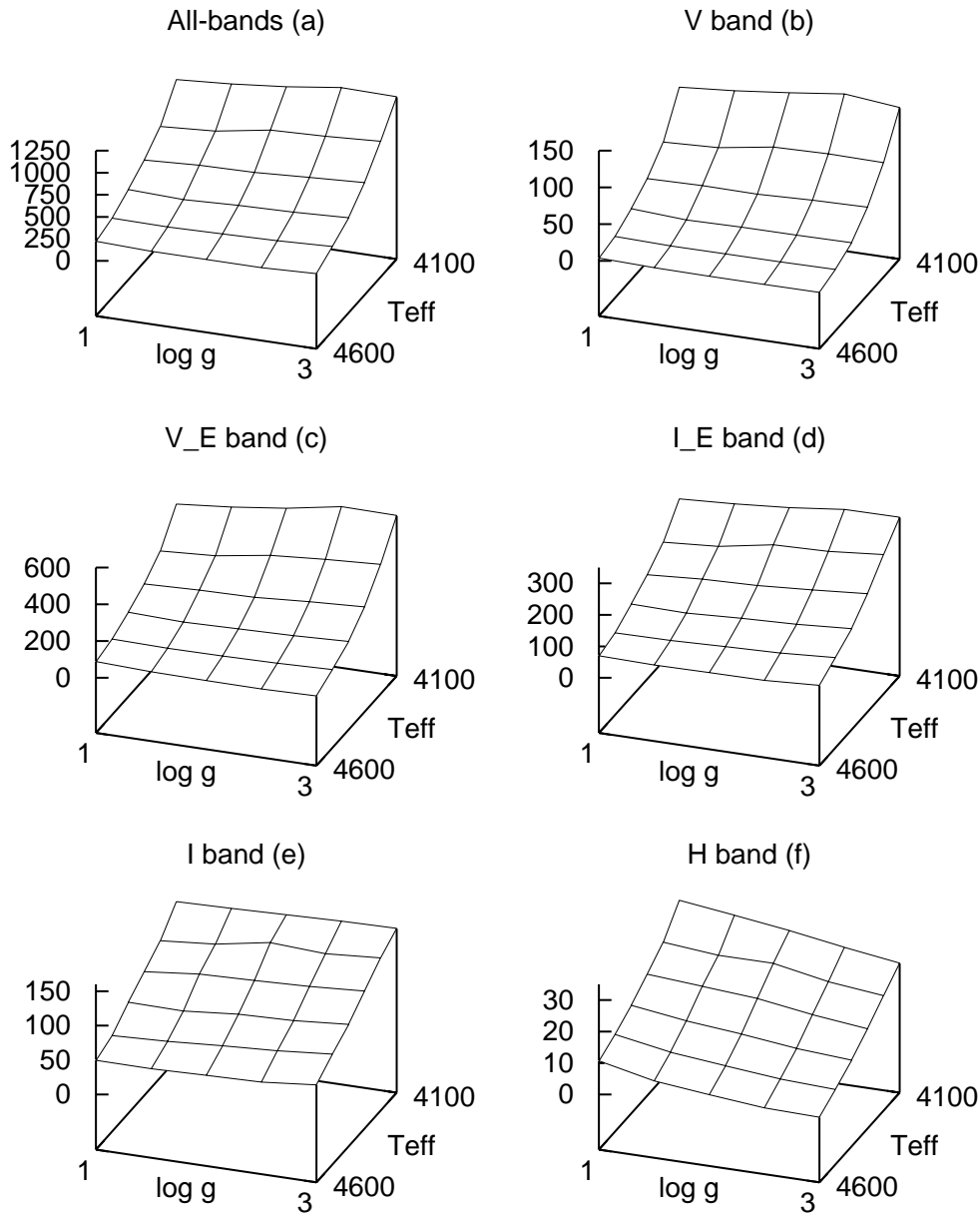


FIG. 5.— $\chi^2$  surfaces of the microlens-Next<sup>2</sup>Gen comparison at fixed  $[\text{Fe}/\text{H}] = +0.3$  for (a) all bands, (b) the  $V$  band, (c) the  $V_E$  band, (d) the  $I_E$  band, (e) the  $I$  band, and (f) the  $H$  band. All the surfaces share the same general shape: monotonic dependence on  $T_{\text{eff}}$  and  $[\text{Fe}/\text{H}]$ , with a favored value of  $\log g$ . With the exception of very low  $\log g$  (0.0–0.5),  $\chi^2$  varies most in  $T_{\text{eff}}$ , with variations over  $\log g$  and  $[\text{Fe}/\text{H}]$  (not shown) being much lower.

include searching for a solution over  $d$  and  $q$ . The PLANET-only solution is located at the same  $(d, q)$  as the combined solution. Moreover, as discussed in § 4.6.1, removing the EROS data does not appreciably change the limb-darkening profiles found from the remaining (i.e., PLANET) data. However, we find a very different result for the EROS-only solution. This is located at a  $(d, q)$  of (1.94, 0.77) that is (0.0, 0.02) away from the combined solution. The EROS-only solution has a  $\chi^2$  that is 75 lower than the  $\chi^2$  of the EROS bands at the combined solution. The derived stellar brightness profile is flat across the inner half of the star, then drops dramatically toward the limb. The ratio of intensities of the center to the limb are similar to that of the  $V$  band, but the shape of the EROS profiles are very different. The EROS-only profiles are a much better match to the Next<sup>2</sup>Gen models than the EROS profiles

derived at the all-band geometry. The  $\chi^2$  of the MPM drops from 387 and 251 to 174 and 69 for the  $V_E$  and  $I_E$  bands, respectively. However, the profiles from the EROS-only solution are still not actually consistent with any of the Next<sup>2</sup>Gen models, since  $\chi^2_{\text{min}} = 87$  and 32 in the two EROS bands.

Such a major inconsistency is a potentially serious problem. How can the previously described disagreement between atmospheric models and microlensing be trusted if the microlensing can produce such different fits? We argue that this problem can be resolved in the following manner: (1) we identify the feature that has the most diagnostic power with regards to the limb darkening, the caustic exit; (2) we show how the EROS data sets do not well determine this feature, although the combination of EROS and SAO  $H$ -band data sets do; and (3) we investigate whether the

large formal difference in  $\chi^2$  between the EROS-only and all-band geometries represents a failure of the model or of the data and what the consequences of that failure are.

We first examine the region from which we receive the most information about the limb darkening, near the caustic exit. This region is shown in Figure 6. An accurate estimate of the caustic-exit time is essential for determining the amount of darkening on the extreme limb. This can be illustrated by thinking about the data points just outside the true caustic exit. If the caustic exit were thought to occur later than it actually does, these points would be thought to be inside the caustic. Their faintness would therefore imply that the part of the star undergoing the strongest differential magnification (the limb) had very low surface brightness. On the other hand, if the caustic exit is recognized to occur

before these points, their faintness is properly attributed to the fact that there are no additional images of the source, i.e., the source lies entirely outside the caustic.

This is exactly the issue with respect to the disagreement between the PLANET-only and EROS-only geometries. As Figure 6 shows, the EROS-only geometry places the caustic exit at a later time, which implies greater limb darkening. We therefore investigate how well the caustic-exit time is determined by the all-band data set and what the source of this discrepancy is.

First we note that the time of the caustic exit is essentially determined from the combination of the SAAO  $H$ -band data and the EROS data: the  $H$ -band data show an approximately linear fall toward the caustic exit, and this fall must break very close to the best-fit caustic exit if the magnification curve

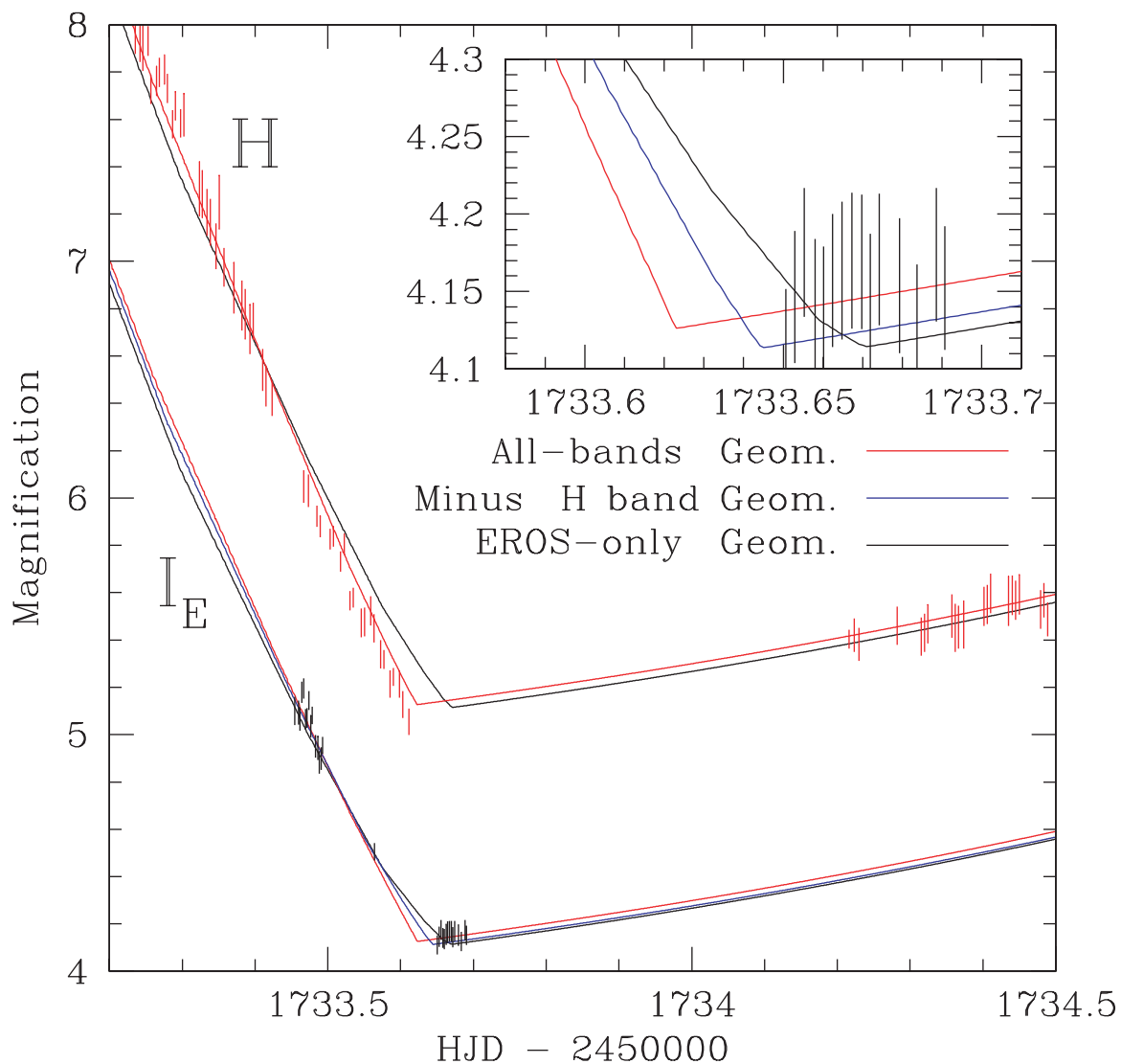


FIG. 6.—Magnification for EROS BLG-2000-5 in the  $H$  and  $I_E$  bands. The  $H$  band has been shifted by +1 in magnification to separate it from the  $I_E$  band. Also shown are the error bars for the SAAO  $H$ -band and EROS  $I_E$ -band data points. The magnification for each data point has been reconstructed using the observed flux, source flux, blend flux, and seeing correction, the last three of which are derived from the all-band solution. These three quantities are very stable and do not appreciably change between microlens models. The black lines show the predicted light curve derived from the geometry at the EROS-only solution, the blue line shows the predicted light curve from the geometry at the solution containing all data sets except the  $H$  band, and the red lines show the predicted light curve for the geometry at the all-band solution. *Inset*: Expanded view of the  $I_E$  caustic-exit region. Note that the  $I_E$ -band points could support either prediction, while the  $H$ -band points strongly favor the all-band solution.

is to remain continuous and still pass through the EROS  $I_E$  points. See Figure 6. Thus, the caustic-exit time can be specified virtually without reference to any model.

Even if the EROS points are eliminated from the fit, the best-fit light curve based on only PLANET data still passes through these EROS points and intersects the linearly falling SAAO  $H$ -band light curve at almost exactly the same caustic exit. Because the PLANET points that fix the post-exit magnification start up about 10 hr after the exit, when the magnification has already started to rise, this determination of the caustic exit is somewhat model dependent. However, the model dependence is quite weak. Hence, we have two independent and robust lines of evidence fixing the caustic-exit time, and for this reason we have high confidence in the result.

Nevertheless, it remains somewhat puzzling why the EROS-only solution prefers a later time. From Figure 6, it is clear that the EROS data near the caustic exit do not themselves strongly prefer one solution over the other. Hence, this discrepancy must be rooted in other parts of the light curve: either the EROS data have systematic errors elsewhere in the light curve, or the model does not exactly reproduce the true light curve.

To distinguish between these possibilities, we first exclude the  $H$ -band data and refit the light curve. The result is shown by the blue line in Figure 6, which is between the EROS-only solution and the PLANET-only solution. Clearly the pressure toward a late caustic exit is not coming from the EROS data alone. To verify this, we eliminate the  $H$  band, the remaining SAAO bands, and the EROS data. The resulting exit, which lies almost on top of the blue line of the minus- $H$ -band geometry, also lies halfway between the PLANET-only and EROS-only values. Since the problem is not restricted to one data set, we conclude that the model must imperfectly predict the data elsewhere in the light curve. We have attempted to isolate this discrepancy by using various techniques but have not succeeded because the effect is extremely small and manifests itself only when data far from the caustic exit are used to predict the caustic-exit time. As with any such extrapolation, caustic-exit predictions in particular (Albrow et al. 1999b), small errors can be vastly magnified when predicting distant effects.

We must also determine how much the fit to the caustic region (and so the limb-darkening measurement) is being distorted on account of data far away. To do so, we decrease the error by a factor of 10 on the group of  $H$ -band points just before the caustic exit. This should increase the relative importance of this region to the overall fit and be able to tell us to what extent the light curve near the caustic exit is being influenced by data far away. The caustic exit shifts slightly to an earlier time, as we should expect given that data far from the caustic tends to shift it to later times. This shift, however, does not produce substantial changes in the limb-darkening curves, shifting them by  $1\sigma$ – $1.5\sigma$  on average. We conclude that the caustic exit is very well determined, and the discrepancies related to it do not significantly affect the limb-darkening determinations.

#### 4.6.3. Fitting Routine

It is unlikely that our fitting routine is the source of the conflict. We fitted all the data simultaneously, so one would

expect that any systematic effects would have to be present in all bands. The limb-darkening curves in these five bands are all internally consistent with each other. Without outside information, the microlensing routine found that the amount of limb darkening increases with decreasing wavelength, starting from a very flat profile in  $H$  band and progressing through  $I$ ,  $I_E$ , and  $V_E$  to a relatively steep  $V$ -band profile (see Fig. 1). Even the relative amounts of limb darkening are roughly correct. The mean wavelength of the  $I_E$  band is 14% of the way between that of the  $I$  and  $V$  bands (Afonso et al. 2000), and indeed, the  $I_E$ -band limb-darkening profile is very similar to the  $I$ -band profile. The mean wavelength of the  $V_E$  band is 27% of the way between  $V$  and  $I$  (Afonso et al. 2000), and the  $V_E$  profile is more like the  $V$ -band profile than the  $I$ -band profile, and as expected the degree of similarity between the  $V_E$  and  $V$  profiles does not match that between the  $I_E$  and  $I$ .

It is also unlikely that statistical fluctuations could be the cause of the disagreement between the microlens data and the atmospheric models. We note that the disagreement for just the  $V$ ,  $I$ , and  $H$  bands with both the ATLAS and Next<sup>2</sup>Gen models are substantially greater than  $\chi^2 = 100$ . Even at  $\chi^2 = 100$ , the probability of random fluctuations being responsible is  $\sim 10^{-19}$ .

#### 4.6.4. Atmospheric Models

Figure 7 compares the  $I$ -band limb darkening derived from microlensing with a suite of ATLAS atmospheric models all at the same  $\log g = 2.5$  and  $[M/H] = +0.3$  but with different temperatures. A striking feature of this figure is that all the atmospheric models go through a single point, one that the microlensing model does not go through. This exact feature is also present in the Next<sup>2</sup>Gen models shown in Figure 8. This common feature is not apparent when the limb-darkening curves are normalized in the usual  $(c_\lambda, d_\lambda)$  formalism. It appears only when limb-darkening curves are plotted to conserve total flux as in equation (1). Such a fixed point would be a generic feature of any single-parameter limb-darkening profile of the form

$$S(r) = K[1 + af(r)], \quad (5)$$

where  $r = \sin(\vartheta)$  is the normalized angular radius,  $K$  is the normalizing factor such that the profile has unit flux,  $a$  is the limb-darkening coefficient, and  $f(r)$  is an arbitrary function of  $r$ . This fixed point is located at  $r_{\text{fix}} = f^{-1}[2 \int_0^1 f(r')r' dr']$ . For example, for linear limb-darkening of the form  $f(r) = 1 - (1 - r^2)^{1/2}$ ,  $r_{\text{fix}} = 5^{1/2}/3 \sim 0.745$ .

However, such a fixed point is not required in a two-parameter limb-darkening law such as we use. Nonetheless, it still appears in the atmospheric models. What is more, the limb-darkening profile for the Sun (the only star in the sky with better measured limb darkening than EROS BLG-2000-5) also passes through this point that all the atmospheric models share; that is, the models all carry a common feature that is also present in the Sun but does not exist in the giant EROS BLG-2000-5.

Heyrovský (2000) was the first to find these fixed points, specifically for the standard linear limb-darkening law and for a single-parameter principal component analysis (PCA). Heyrovský (2000) notes that the solar data can be reproduced using just the first component of a PCA basis derived from cool-star models. He argues for a physical origin of this effect, namely, that both cool giants and the Sun share a

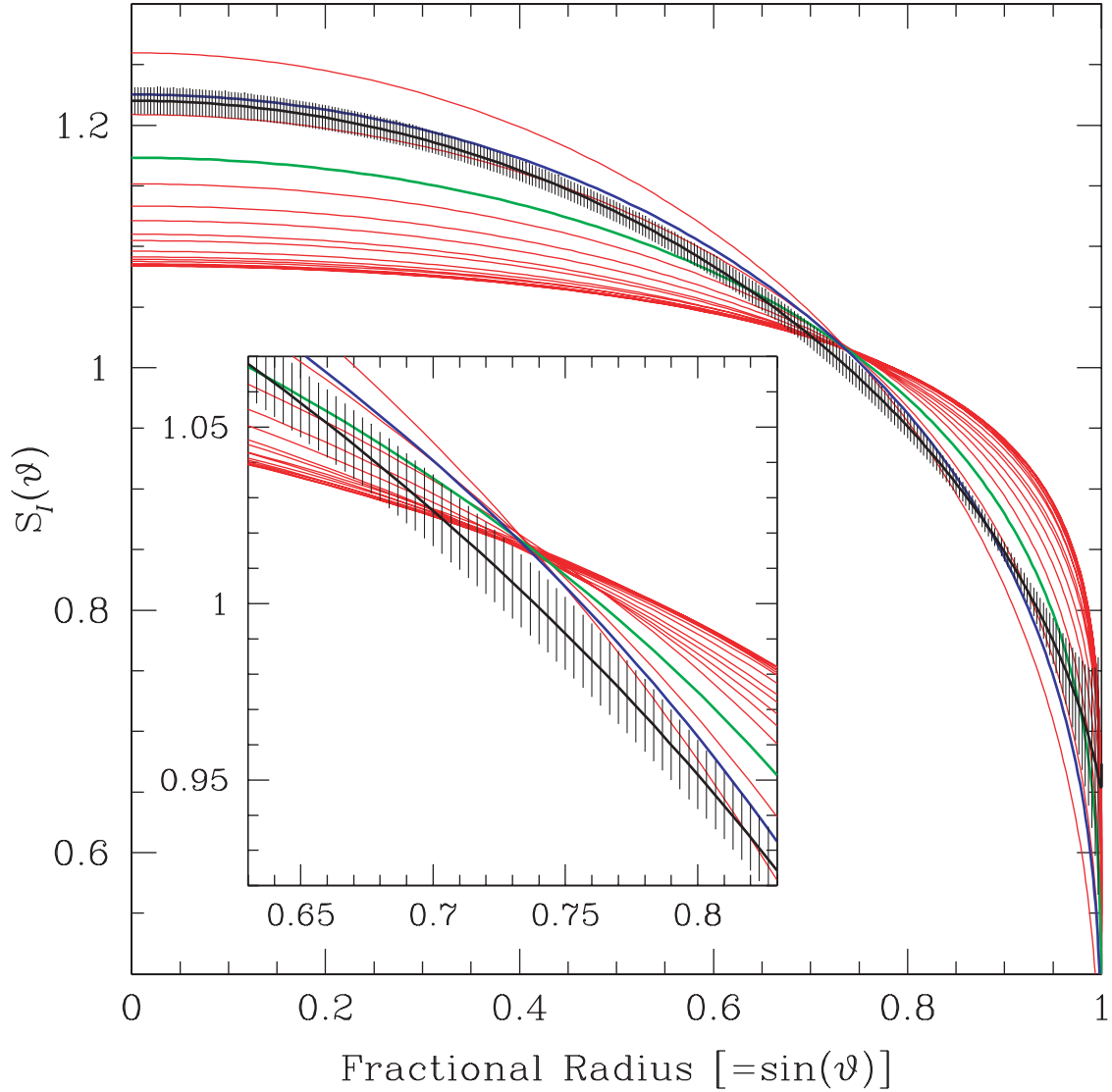


Fig. 7.—Brightness profile in the  $I$  band. The black line and shading are EROS BLG-2000-5 and its associated  $3\sigma$  error envelope. The red lines give ATLAS models (Claret 2000) at  $\log g = 2.5$  and  $[M/H] = +0.3$  for  $T_{\text{eff}}$  between 3000 and 18,000 K, in 1000 K increments with the lowest-temperature model the most highly limb darkened (i.e., the curve that is the brightest in the center and dimmest at the limb). The blue line corresponds to the best-fit ATLAS model at  $T_{\text{eff}} = 4500$  K,  $\log g = 3.0$ , and  $[M/H] = -0.3$ . Also shown is the  $I$ -band curve of the Sun in green. As can be seen, there is a point that all the model curves share with the Sun at approximately  $(r, S_I) = (0.74, 1.02)$ . This fixed point, which is not shared by the microlensing-determined profile, is not apparent in the  $(c_\lambda, d_\lambda)$  formalism.

primary opacity source:  $\text{H}^-$ . We conjecture that these models, which are capable of producing fits to the Sun, incorporate physics that is completely applicable only to the solar regime. This may relate to opacity or to some other physical mechanism. Whatever the source of the discrepancy, this deserves further study.

#### 4.6.5. ATLAS-Next<sup>2</sup>Gen Comparison

The  $\chi^2$  surfaces for the ATLAS and Next<sup>2</sup>Gen models are shown in Figures 3 and 5. As there are three input parameters,  $T_{\text{eff}}$ ,  $\log g$ , and metallicity for each model, we hold the least important constant, and show  $\chi^2$  versus the other two. This results in two fairly similar-looking surfaces. In both cases,  $T_{\text{eff}}$  is the most important parameter in determining  $\chi^2$ , with the metallicity and surface gravity playing far more subordinate roles. Additionally, while the true  $\chi^2_{\text{min}}$  for the

Next<sup>2</sup>Gen models is beyond the range in parameter space that we investigated, the flattening of the  $\chi^2$  surface indicates that it is not very far away. Both the ATLAS and the Next<sup>2</sup>Gen models are most consistent with a star of  $T_{\text{eff}} \sim 4700$  K,  $\log g = 2.5\text{--}3.0$ , and metallicity around  $-0.3$ . Finally, we are able to directly compare these two atmospheric models at  $T_{\text{eff}} = 4000$  and  $4500$ ,  $\log g = 2.5$ , and metallicity  $+0.3$ . Using our error bars as the metric of comparison, the worst disagreement is  $\sim 3\sigma$ , for  $r < 0.3$  at  $T_{\text{eff}} = 4500$ . In all other regions the two profiles tend to disagree by  $\lesssim 1\sigma$ .

#### 4.6.6. Model Atmosphere-Microlens Profile Comparison

As we have just shown in § 4.6.5, the atmospheric models both seem to prefer a K1 star. It is therefore important to ask whether our observations are biased and we are

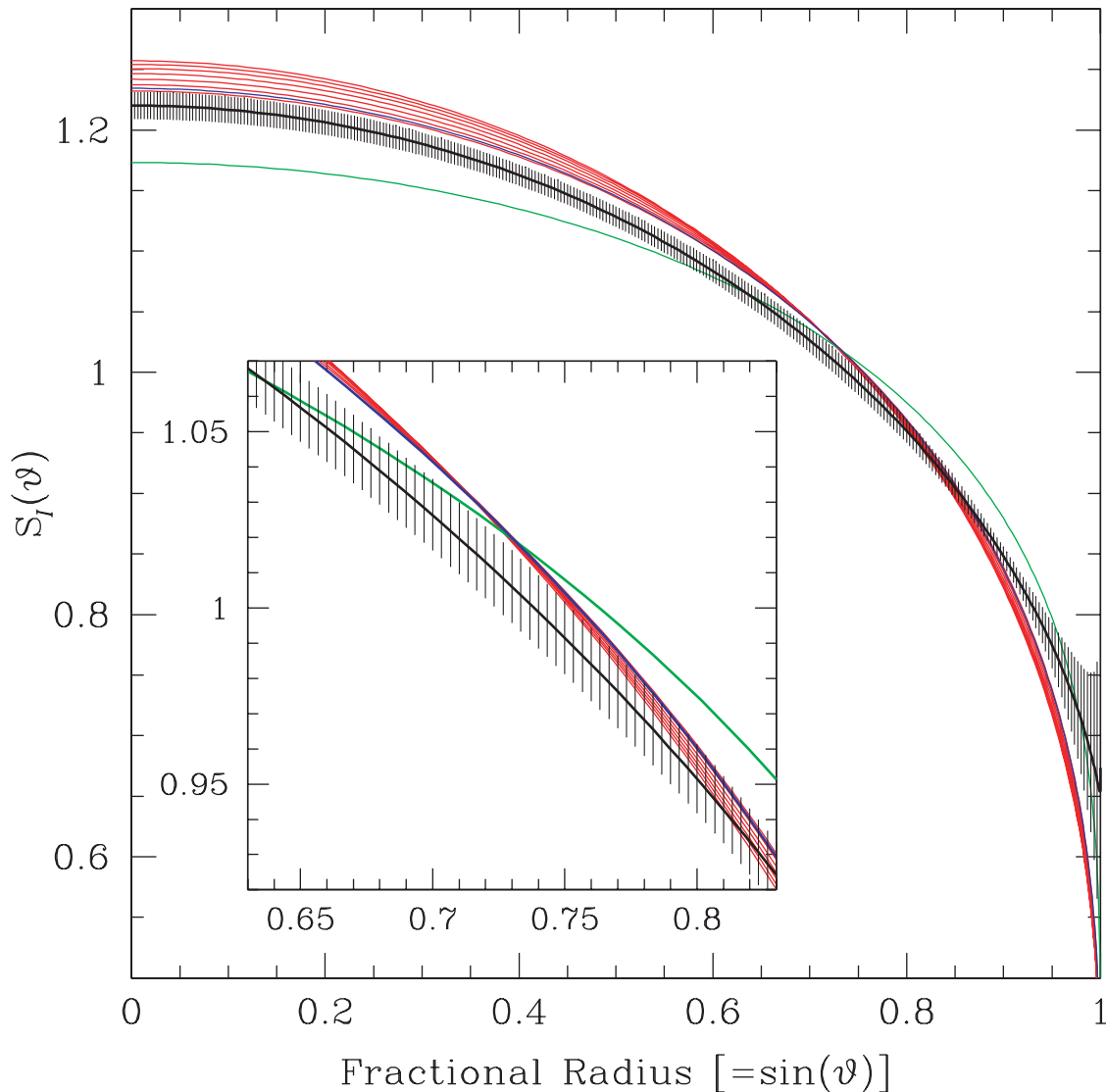


FIG. 8.—Brightness profile in the  $I$  band. The black line and shading are EROS BLG-2000-5 and its associated  $3\sigma$  error envelope. The red lines give Next<sup>2</sup>Gen models at  $\log g = 2.5$  and  $[M/H] = +0.3$  for  $T_{\text{eff}}$  between 4000 and 4600 K, in 100 K increments with the lowest-temperature model the most limb darkened (i.e., the curve that is the brightest in the center and dimmest at the limb). The blue line corresponds to the best-fit Next<sup>2</sup>Gen model at  $T = 4600$  K,  $\log g = 2.5$ , and  $[M/H] = -0.25$ . Also given is the  $I$ -band curve of the Sun in green. As can be seen, there is a point that all the model curves share with the Sun at approximately  $(r, S_I) = (0.73, 1.02)$ . This fixed point is the same as the one that the ATLAS models share (but the microlensing-determined profiles do not) and is not apparent in the  $(c_\lambda, d_\lambda)$  formalism.

expecting the wrong type of star. In principle, differential extinction across the field could redden the star more than the clump stars against which it is calibrated (see Fig. 10 of An et al. 2002), thus affecting our photometric estimate of its intrinsic color. However, the spectroscopic analysis yields a source temperature similar to the one we find photometrically.

One should note that reddening has the effect of shifting the observed bands. We find, however, that the measured extinction for EROS BLG-2000-5 [ $E(V-I) = 1.3$ ] shifts the mean wavelength of the  $I$  bandpass by only  $+100$  Å. This shift is about 28% of the difference between the mean wavelengths of  $I$  and  $I_E$  and only 4% of the difference between  $I$  and  $V$ . Comparing Figures 7 and 1, one sees that it cannot account for differences between the observations and the atmospheric models. This is partly because the magnitude of the effect is too small and partly because it causes a shift in the wrong direction.

## 5. CONCLUSION

The observational limb darkening found from microlensing formally disagrees with the limb darkening derived from atmospheric models by many standard deviations. We have argued that this difference is unlikely to be the result of the observations, but it is more likely due to something related to the atmospheric models. It is possible that these models include physics that is not applicable in all surface gravity regimes. It is a testament to the theoretical models that they approximate reality in several bands without any previous physical data. We hope that now that giant stars have a calibration point, much like dwarfs have from the Sun and supergiants have from interferometry, stellar models can continue to improve in all stellar regimes.

We would like to thank Joachim Wambsganss for his comments on this manuscript. We would also like to thank

Amelia Stutz for her work in reducing the *H*-band data. We thank the EROS collaboration for providing us with their data in advance of its publication. We gratefully acknowledge donations to the Mount Canopus Observatory by David Warren. D. L. F. and A. G. were supported by grant AST 02-01266 from the NSF. Some of

the observations were obtained by D. L. D. under NASA grant NAG-10678. B. S. G. was supported by NASA through a Hubble Fellowship grant from the Space Telescope Science Institute, which is operated by the Association of Universities for Research in Astronomy, Inc., under NASA contract NAS 5-26555.

## REFERENCES

- Afonso, C., et al. 2000, *ApJ*, 532, 340  
———. 2001, *A&A*, 378, 1014  
———. 2003, *A&A*, in press  
Alard, C. 2000, *A&AS*, 144, 363  
Albrow, M. D., et al. 1999a, *ApJ*, 512, 672  
———. 1999b, *ApJ*, 522, 1022  
———. 2000, *ApJ*, 534, 894  
———. 2001, *ApJ*, 549, 759  
An, J. H., et al. 2002, *ApJ*, 572, 521  
Ansari, R. 1996, *Vistas Astron.*, 40, 519  
Brown, T. M., Charbonneau, D., Gilliland, R. L., Noyes, R. W., & Burrows, A. 2001, *ApJ*, 552, 699  
Burns, D., et al. 1997, *MNRAS*, 290, L11  
Castro, S. M., Pogge, R. M., Rich, R. M., DePoy, D. L., & Gould, A. 2001, *ApJ*, 548, L197  
Charbonneau, D., Brown, T. M., Latham, D. W., & Mayor, M. 2000, *ApJ*, 529, L45  
Claret, A. 2000, *A&A*, 363, 1081  
Hauschildt, P. H., Allard, F., Ferguson, J., & Baron, E. 1999a, *ApJ*, 512, 377  
Hauschildt, P. H., Allard, F., Ferguson, J., Baron, E., & Alexander, D. R. 1999b, *ApJ*, 525, 871  
Heyrovský, D. 2000, Ph.D. thesis, Harvard Univ.  
Pierce, A. K., & Waddell, J. H. 1961, *MmRAS*, 63, 89  
Popper, D. M. 1984, *Mitt. Astron. Ges.*, 62, 19  
———. 1985, in *IAU Conf. Ser. 111, Calibration of Fundamental Stellar Quantities* (Dordrecht: Reidel), 81  
Schechter, P. L., Mateo, M., & Saha, A. 1993, *PASP*, 105, 1342  
Wittkowski, M., Hummel, C. A., Johnston, K. J., Mozurkewich, D., Hajian, A. R., & White, N. M. 2001, *A&A*, 377, 981